Applied Catalysis B: Environmental 193 (2016) 1–8

Contents lists available at ScienceDirect

Applied Catalysis B: Environmental

journal homepage: www.elsevier.com/locate/apcatb

Cobalt-nitrogen-doped ordered macro-/mesoporous carbon for highly efficient oxygen reduction reaction

Tingting Sun [a], Lianbin Xu [a,*], Shengyu Li [a], Wenxia Chai [a], Yan Huang [a], Yushan Yan [b], Jianfeng Chen [a]

[a] State Key Laboratory of Organic–Inorganic Composites, Beijing University of Chemical Technology, Beijing 100029, China
[b] Department of Chemical and Biomolecular Engineering, University of Delaware, Newark, DE 19716, United States

ARTICLE INFO

Article history:
Received 18 December 2015
Received in revised form 24 February 2016
Accepted 5 April 2016
Available online 8 April 2016

Keywords:
Co-N-doping
Ordered macro-/mesoporous carbon
Dual-templating synthesis
Electrocatalyst
Oxygen reduction reaction
Durability

ABSTRACT

Cobalt-nitrogen-doped three-dimensionally (3D) ordered macro-/mesoporous carbons (Co-N-OMMCs) have been fabricated through a dual-templating synthesis approach in a one-pot controllable procedure by the use of silica colloidal crystal (opal) as a macroporous mold and triblock copolymer Pluronic F127 as a mesoporous template. The optimal catalyst (Co-N-OMMC-0.6) exhibits comparable catalytic activity but much higher durability and tolerance of methanol in comparison with the commercial 20 wt% Pt/C catalyst for oxygen reduction reaction (ORR) in an alkaline medium. The remarkable ORR electrocatalytic performance of the Co-N-OMMC-0.6 is ascribed to the homogeneous distribution of abundant Co-N_x active sites, as well as the large surface area and efficient mass/charge transport from the unique structure combining well-ordered bicontinuous mesopores with 3D interconnected periodic macropores.

1. Introduction

In the face of the looming global energy crisis, extensive research has focused on energy conversion and storage systems [1,2]. The oxygen reduction reaction (ORR) plays a critical role in various energy conversion devices, including fuel cells and metal–air batteries [3–8]. However, the reaction is kinetically sluggish, and thereby it is necessary to explore effective electrocatalysts to reduce the overpotential and improve the ORR performance. Up to now, Pt and its alloys are still considered the most efficient ORR catalysts [9–11], but the high cost and limited supply of precious metals severely hamper their widespread utilization [12–14]. Thus, the global research efforts have been devoted to the search for alternative non-precious-metal catalysts with competitive performance to boost the ORR [15–20].

Currently, metal-free nitrogen doped carbon materials are among the most promising non-precious-metal catalysts for ORR because of their good activity, low cost, high stability and environmental friendliness [21,22]. A variety of N-doped carbon materials, such as porous carbon nanofibers [23], carbon nanotube/nanoparticle composite [24], mesoporous graphene [25], ordered mesoporous carbon [26,27], and hierarchical macro-/mesoporous carbon (HMMC) [28] have been prepared and displayed high ORR catalytic performance. Among them, N-doped HMMC materials are receiving growing attention due to their exceptional architecture advantages, such as high surface area from the mesopores and efficient mass transport from the interconnected macropores [29]. Although some breakthroughs have been achieved by using optimized synthetic strategies and selecting proper nitrogen and carbon sources [30–32], obtaining the N-doped HMMC catalysts with comparable ORR catalytic performance to commercial Pt/C catalysts still remains a challenge.

The addition of certain transition metal, such as Co, to the N-doped HMMC materials has been demonstrated to be an effective way to produce catalysts with improved ORR performance [33,34]. Li et al. synthesized hierarchical interconnected macro-/mesoporous Co-containing N-doped carbon by using poly(vinyl alcohol) (PVA) hydrogel-based composites as in situ templates followed by a carbonization process [35] and Qiao et al. fabricated hierarchical yolk-shell Co, N co-doped porous carbon microspheres based on a facile template-free hydrothermal method with a subsequent pyrolysis [36]. However, these attempts lack the control of the uniformity and ordering of the macropores and mesopores,

Abbreviations: Co-N-OMMCs, cobalt-nitrogen-doped three-dimensionally (3D) ordered macro-/mesoporous carbons; ORR, oxygen reduction reaction; HMMC, hierarchical macro-/mesoporous carbon; DCDA, dicyandiamide; LSVs, linear sweep voltammograms; CVs, cyclic voltammograms; RHE, reversible hydrogen electrode.

* Corresponding author.
E-mail addresses: xulb@mail.buct.edu.cn, lbxu99@163.com (L. Xu).

http://dx.doi.org/10.1016/j.apcatb.2016.04.006
0926-3373/

which may still limit the mass transport through the porous structures and then restrain the access of reactants to the active sites. To further enhance the ORR performance of the Co-N-doped HMMC materials, a promising strategy is to construct hierarchical structure with ordered interconnected macropores and mesopores, since the ordered bicontinuous pores can provide a shorter molecule/ion diffusion length in the reaction solution, resulting in more efficient diffusion of reagents compared with the disordered ones.

The dual-templating synthesis approach applying cooperative colloidal crystal (opal) and surfactant templating techniques provides an efficient way to fabricate hierarchical materials with three-dimensionally (3D) ordered macro- and mesoporous structure, which would allow for significantly enhanced active-site accessibility and extremely fast mass diffusion [37,38]. Herein, we first demonstrated the fabrication of Co-N-doped 3D ordered macro-/mesoporous carbons (Co-N-OMMCs) via a one-pot controllable method by using silica opal as a hard template, amphiphilic triblock copolymer Pluronic F127 as a mesopore-structure-directing agent (soft template), and phenolic resol (M_w <500), dicyandiamide (DCDA) and $Co(NO_3)_2{\cdot}6H_2O$ as the C, N and Co sources, respectively. In addition, the ORR catalytic properties of the prepared Co-N-OMMC catalysts with various Co content are investigated, and it is found that the optimal Co-N-OMMC displays an outstanding electrocatalytic performance toward ORR.

2. Experimental

2.1. Chemicals

Triblock copolymer Pluronic F127 (M_w = 12.5 K, PEO-PPO-PEO), dicyandiamide (DCDA, 99%) and Nafion solution (5 wt%) were purchased from Sigma-Aldrich Co. Phenol (99%), sodium hydroxide (NaOH, 96%), formaldehyde solution (37%), cobalt nitrate hexahydrate ($Co(NO_3)_2{\cdot}6H_2O$, 99%), tetraethoxysilane (TEOS, 98%), potassium hydroxide (KOH, 98%), hydrofluoric acid (HF, 40%), and ethanol (99.7%) were obtained from Beijing Chemical Works. All chemicals were used as received without further purification.

2.2. Synthesis of silica colloidal crystal (opal)

Silica opal was prepared by published methods [39]. Monodisperse silica spheres with a diameter of ca. 290 nm was initially prepared from hydrolysis of TEOS. The spheres were then formed into close-packed lattices through a sedimentation process over several months. This precipitate was then sintered at 120 °C for 2 days and then 750 °C for 4 h, producing a robust opalescent piece that could be readily cut into smaller sections.

2.3. Synthesis of resol

Resol was prepared by the method reported by Meng et al. previously [40]. Specifically, 10 g phenol was melt at 40–42 °C, then 2.13 g 20% NaOH aqueous solution was added dropwise over 10 min under stirring. Next, 17.7 g formaldehyde solution was added dropwise and the temperature was raised to 70 °C. The mixture was heated and stirred for 60 min and then cooled to room temperature. After that, the pH of the solution was adjusted with 0.6 M HCl solution to neutral (7.0). Water was then removed under vaccum below 50 °C. The synthesized resol (M_w <500) was dissolved in ethanol before use.

2.4. Synthesis of the Co-N-doped 3D ordered macro-/mesoporous carbons (Co-N-OMMCs)

1.0 g F127 and 1.0 g DCDA were first dissolved in a mixture of 20 g ethanol and 10 g water containing different amounts (0.3–0.9 g) of $Co(NO_3)_2{\cdot}6H_2O$ under continuous stirring for 30 min. 5.0 g of resol ethanol solution (20 wt%) was then added and stirred for another 30 min. Next, 0.2 g acetyl acetone was added dropwise into the solution under stirring. After that, 1.0 g of the silica opal was immersed in the above precursor solution for 1 h at room temperature, and then kept at 50 °C for 6 h. Subsequently, the impregnated composites were carefully taken out to evaporate the solvent at 50 °C for 4 h, followed by further heating at 100 °C for 24 h for thermosetting. The resulting silica/PF/F127/DCDA/$Co(NO_3)_2$ (PF: phenolic formaldehyde) composites were then heated under N_2 atmosphere at 350 °C for 2 h at a heating rate of 1 °C min^{-1}, and at 5 °C min^{-1} rising to 900 °C, followed by a 2 h soak for further carbonation. Finally, the freestanding Co-N-OMMCs were obtained by removing the silica opal with a 5 wt% HF solution (24 h). By varying the mass ratio of $Co(NO_3)_2{\cdot}6H_2O$ to resol, a series of samples were synthesized. These samples are simply denoted as Co-N-OMMC-*x*, where *x* is the mass ratio of $Co(NO_3)_2{\cdot}6H_2O$ to resol. For comparison, N-doped 3D ordered macro-/mesoporous carbon (N-OMMC) was also prepared by the same fabrication procedure for the Co-N-OMMCs but without adding $Co(NO_3)_2{\cdot}6H_2O$ in the precursor.

2.5. Physical characterization

Scanning electron microscopy (SEM) images were obtained on a Hitachi S-4700 FEG scanning electron microscope. Transmission electron microscopy (TEM) was carried out on a JEOL JEM-3010 transmission electron microscope operating at 200 kV. The nitrogen adsorption and desorption isotherms were measured at 77 K using Micromeritics ASAP 2010 apparatus. Powder X-ray diffraction (XRD) data were collected on a Rigaku D/max 2500 VB2+/PC diffractometer with Cu-Kα radiation (λ = 1.5418 Å). X-ray photoelectron spectroscopic (XPS) analysis was carried out on an ESCALAB 250 X-ray photoelectron spectrometer with a monochromatic Al Kα radiation source.

2.6. Electrochemical tests

The electrochemical tests were conducted in a conventional three-electrode cell on a potentiostat/galvanostat (Reference 600, Gamry Instruments) with a Pt foil as the counter electrode, a double junction Ag/AgCl (saturated KCl) as the reference electrode, and a glassy carbon (GC) rotating disk electrode (5 mm in diameter, Pine Instruments) modified with various catalysts as the working electrode. The catalyst ink was fabricated by dispersing 5 mg of as-prepared catalyst or commercial Pt/C into a solution containing water, isopropanol, and Nafion solution (5 wt%) at a volume ratio of 3:1:0.16 by at least 30 min sonication to generate a homogeneous dispersion. Then, 10 μL of the above prepared catalyst ink was deposited on the pre-polished GC electrode (catalyst loading: ~0.22 mg cm^{-2}) and dried in air completely. A 0.1 M KOH aqueous solution was served as the electrolyte.

All potentials in the paper were normalized to the reversible hydrogen electrode (RHE) using the Nernst equation: $E_{RHE} = E_{Ag/AgCl} + 0.964$. Cyclic voltammograms (CVs) were acquired within a potential range of 0.1–1.3 V vs. RHE at a scan rate of 50 mV s^{-1}. Prior to the electrochemical measurement, the electrolyte was saturated with oxygen or nitrogen by bubbling O_2 or N_2 for at least 30 min. The electrode was cycled at least 10 times before recording the data. Linear sweep voltammograms (LSVs) for ORR were acquired in O_2-saturated 0.1 M KOH from 0.1 to 1.2 V (vs. RHE) at a scan rate of 5 mV s^{-1} with varying rotating speed (400–2000 rpm).

Koutecky-Levich plots were collected at various potential for all studied catalysts. The electron transfer numbers (*n*) and kinetic

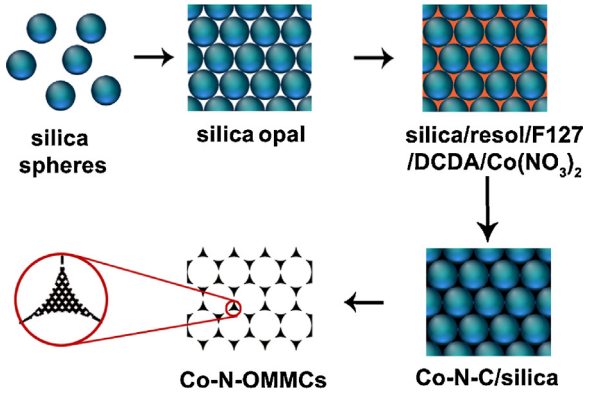

Scheme 1. Schematic of the preparation of the Co-N-doped 3D ordered macro-/mesoporous carbons (Co-N-OMMCs).

currents (j_k) involved in the typical ORR process were calculated on the basis of the Koutecky-Levich equation [41]:

$$\frac{1}{j} = \frac{1}{j_k} + \frac{1}{j_d} = \frac{1}{j_k} + \frac{1}{B\omega^{1/2}}$$

$$B = 0.2nFC_o(D_o)^{2/3}\nu^{-1/6}$$

where j is the measured current density, j_k and j_d are the kinetic and diffusion-limiting current densities, respectively, ω is the rotation speed in rpm, F is the Faraday constant (96,485 C mol^{-1}), D_o is the diffusion coefficient of oxygen in the electrolyte (1.9×10^{-5} cm^2 s^{-1}), ν is the kinetic viscosity of the electrolyte (0.01 cm^2 s^{-1}), and C_o is the bulk concentration of oxygen (1.2×10^{-6} mol cm^{-3}). The constant 0.2 is used when the rotation speed is expressed in rpm.

The chronoamperometry was carried out at a constant potential of 0.60 V vs. RHE in O_2-saturated 0.1 M KOH for at least 25 h. The accelerated degradation testing was performed by running 5000 CV cycles on the electrode between 0.2 and 1.0 V vs. RHE with a scan rate of 100 mV s^{-1}.

3. Results and discussion

3.1. Physical characterization of Co-N-OMMCs

The synthetic procedure for the Co-N-OMMCs using the dual-templating technique is briefly described in Scheme 1. An aqueous/ethanol precursor solution containing resol, DCDA, $Co(NO_3)_2{\cdot}6H_2O$ and F127 was infiltrated into the void space of the silica opal template, and the mesostructure was formed during an evaporation induced self-assembly (EISA) process. Subsequent pyrolysis in N_2 for carbonization, during which DCDA and $Co(NO_3)_2{\cdot}6H_2O$ provided closed N and Co species, while the carbon framework was produced in situ in the voids of the silica opal, leading to the formation of Co-N-C/silica composites. After removal of the silica opal template, freestanding Co-N-OMMCs were obtained.

Fig. 1a shows a typical scanning electron microscopy (SEM) image of a piece of silica colloidal crystal (opal) containing 3D ordered close-packed silica spheres with ~290 nm diameter. The SEM image of Co-N-OMMC-0.6 (Fig. 1b) shows that the inverse opal has an ordered 3D-interconnected macroporous architecture containing open windows between pores. Similar morphologies can also be observed for the N-OMMC and other Co-N-OMMC-x samples (Fig. S1a, c, and e). The inset of Fig. 1b is a higher magnification image of the predominately (111) orientation of the Co-N-OMMC-0.6. The size of the macropores in Co-N-OMMC-0.6 is observed to be ~260 nm, ~10% smaller than the original silica sphere diameter. This contraction is due to the shrinkage of the carbon precursor during the calcination process [42].

Transmission electron microscopy (TEM) and high-resolution TEM (HR-TEM) were employed to obtain more detailed structural information of the Co-N-OMMC samples. Fig. 2a and c show the TEM images of as-prepared Co-N-OMMC-0.6 in the (111) and (211) directions, respectively. The ordered face-centered cubic (fcc) macropores are uniform and the pore size is ~260 nm, which is consistent with the observation from the SEM images. The corresponding HR-TEM images (Fig. 2b and d) reveal that well-defined mesopores are located in the macropore walls, indicating the hierarchically ordered macro/mesoporous structure of the Co-N-OMMC-0.6. The mesopore diameters of all the Co-N-OMMC-x catalysts (Fig. 2b and d, and Fig. S1d and f) are in the range of 10–14 nm, which is slightly larger than that of the N-OMMC (Fig. S1b).

The textural properties of the N-OMMC and Co-N-OMMC-x samples were examined by nitrogen adsorption/desorption isotherms

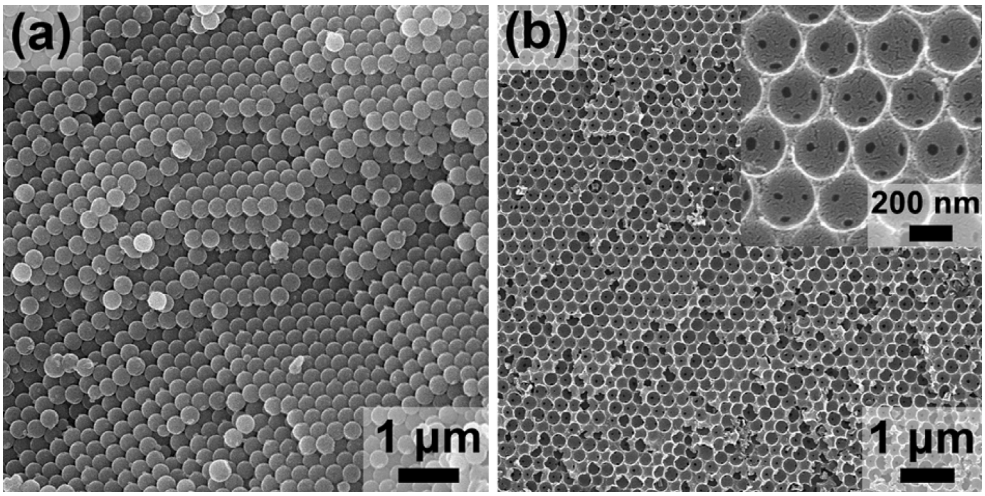

Fig. 1. SEM images of (a) SiO_2 opal consisting of 290 nm diameter spheres, and (b) Co-N-OMMC-0.6 after removal of the opal template, inset: higher magnification with (111) orientation.

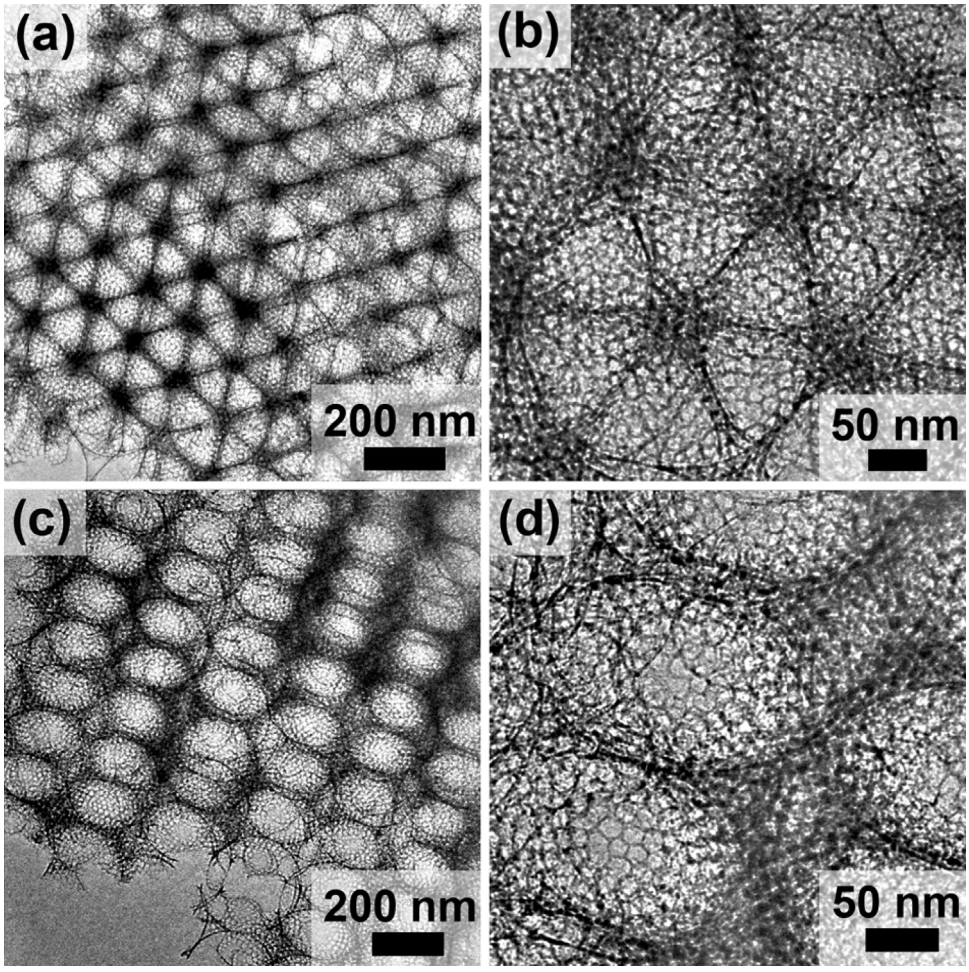

Fig. 2. TEM images of Co-N-OMMCs-0.6 viewed along (a) (111) and (c) (211) directions. (b and d) High-resolution TEM images corresponding to (a and b), respectively, showing the mesoporous structure of Co-N-OMMC-0.6.

Table 1
Texture parameters and elemental composition (at.%) of the as-synthesized materials.

Catalyst	Surface area ($m^2 g^{-1}$)	Average pore size (nm)	Pore volume ($cm^3 g^{-1}$)	C	N	Co	O
N-OMMC	743	9.7	1.85	89.34	4.23	–	6.43
Co-N-OMMC-0.3	679	11.2	1.71	86.79	5.45	0.45	7.31
Co-N-OMMC-0.6	635	11.8	1.65	81.24	8.84	0.98	8.94
Co-N-OMMC-0.9	546	13.5	1.14	78.21	9.64	1.52	10.63

Texture parameters were obtained by BET and PSD, and elemental composition was analyzed by XPS.

(Fig. 3a) and were summarized in Table 1. The characteristic hysteresis behavior indicated these catalysts possess a mesoporous nature [43]. The Brunauer–Emmett–Teller (BET) surface area and pore volume of the Co-N-OMMC-x catalysts were lower than those of the N-OMMC, which could be due to the collapse of mesopores resulting from the acid leaching of possibly existed metal oxide nanoparticles. Notably, Co-N-OMMC-0.6 still possesses a high BET surface area of 635 $m^2 g^{-1}$ and a large pore volume of 1.65 $cm^3 g^{-1}$. The pore size distributions derived from the desorption isotherm by using Barrett–Joyner–Halenda (BJH) method indicate that the average pore diameter of Co-N-OMMC-0.6 is 11.8 nm, which is smaller than that of Co-N-OMMC-0.9 (13.5 nm), but larger than that of N-OMMC and Co-N-OMMC-0.3 (Fig. 3b and Table 1).

The X-ray photoelectron spectroscopy (XPS) analysis was performed to determine the elemental content and chemical state in the N-OMMC and Co-N-OMMC-x samples (Fig. 4a, Table 1). The content of carbon decreases, while the content of nitrogen increases with the adding of cobalt. The high Co/N content and principally high density of active sites of the Co-N-OMMC-0.6 are believed to be highly favorable for enhancing the catalytic properties. The high resolution N1s spectra of N-OMMC and Co-N-OMMC-x catalysts (Fig. 4b) can be divided into four peaks centering at 398.7, 399.8, 401.2, and 403.6 eV, which are attributed to pyridinic N, pyrrolic N, graphitic N, and oxidized-N, respectively [44,45]. The peak centering at 398.7 eV should also include a contribution from nitrogen bound to the metal (Co-N), due to the quite small shift between binding energies of Co-N and pyridinic N [46,47]. The relative percentages of these N functionalities are summarized in Table 2. The addition of transition metals during carbonization process was reported to be beneficial to generating higher contents of pyridinic N or graphitic N, which are generally convinced to play a key role in oxygen reduction [48,49]. These two kinds of active nitrogen are of higher content in Co-N-OMMC-x catalysts compared to N-OMMC, which could be responsible for a higher ORR activity. Remarkably, the amounts of pyridinic-N and graphitic-N raise rapidly upon rising the cobalt content, whereas the pyrrolic-N and oxidized-

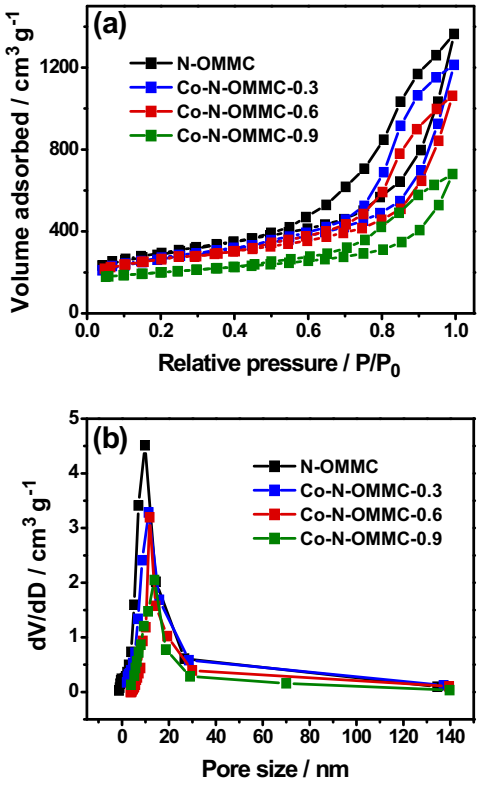

Fig. 3. (a) Nitrogen adsorption/desorption isotherms and (b) corresponding pore size distribution curves for Co-N-OMMCs and N-OMMC.

N content drop significantly, possibly due to the transformation of the pyrrolic-N and oxidized-N to pyridinic-N and graphitic-N at high cobalt content [50]. Fig. 4c shows the Co 2p spectrum of the as-prepared catalysts, and a clear peak at 781.6 can be seen,

Table 2
Content of different N species (%) of the as-synthesized catalysts.

Catalyst	Pyridinic-N/N-Co 398.7 eV	Pyrrolic-N 399.8 eV	Graphitic-N 401.2 eV	Pyridine-N-oxide 403.6 eV
N-OMMC	21.15	18.18	29.03	31.64
Co-N-OMMC-0.3	27.76	15.80	32.02	24.42
Co-N-OMMC-0.6	32.96	13.06	41.26	12.72
Co-N-OMMC-0.9	34.36	11.42	44.58	9.64

indicating that Co is mostly coordinated to nitrogen [51]. Any metal oxide nanoparticles should be dissolved by the etching agent (HF acid), which is consistent with the hardly finding any metal-containing nanoparticles by TEM inspection of Co-N-OMMC-x samples. X-ray diffraction (XRD) pattern further proves the absence of crystalline metal oxide phases (Fig. S2). The Co 2p peaks for Co-N-OMMC-0.6 shift to higher binding energies compared with the other two samples, which can indicate somehow different cobalt electronic states [52].

3.2. Electrochemical activities

The ORR catalytic activity of Co-N-OMMC-0.6 was firstly examined by cyclic voltammetry (CV) conducted in both O_2- or N_2-saturated 0.1 M KOH. As shown in Fig. 5a, Co-N-OMMC-0.6 shows a featureless quasi-rectangular voltammogram in N_2 saturated solution. In contrast, when O_2 is introduced, a well-defined cathodic reduction peak at 0.78 V vs. RHE is observed, indicating that the Co-N-OMMC-0.6 has a pronounced electrocatalytic activity toward the ORR. To gain insight into the ORR process on Co-N-OMMC-x catalysts, rotating-disk electrode (RDE) measurements were then performed in 0.1 M KOH solution saturated with O_2 in comparison with N-OMMC and commercial Pt/C catalyst. The linear sweep voltammograms (LSVs) show that all the three Co-N-OMMC catalysts have higher activity than N-OMMC in terms of half-wave potential and current density (Fig. 5b). Remarkably, Co-N-OMMC-

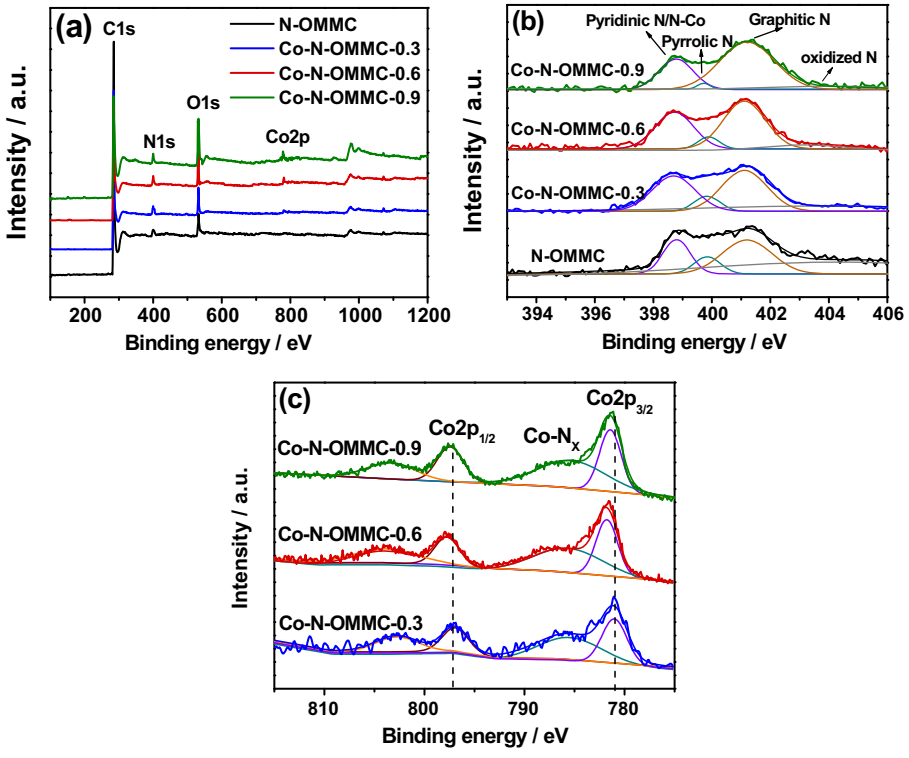

Fig. 4. (a) XPS survey spectra of the Co-N-OMMCs and N-OMMC, and the corresponding high resolution N1s (b) and Co2p (c) spectra of the samples.

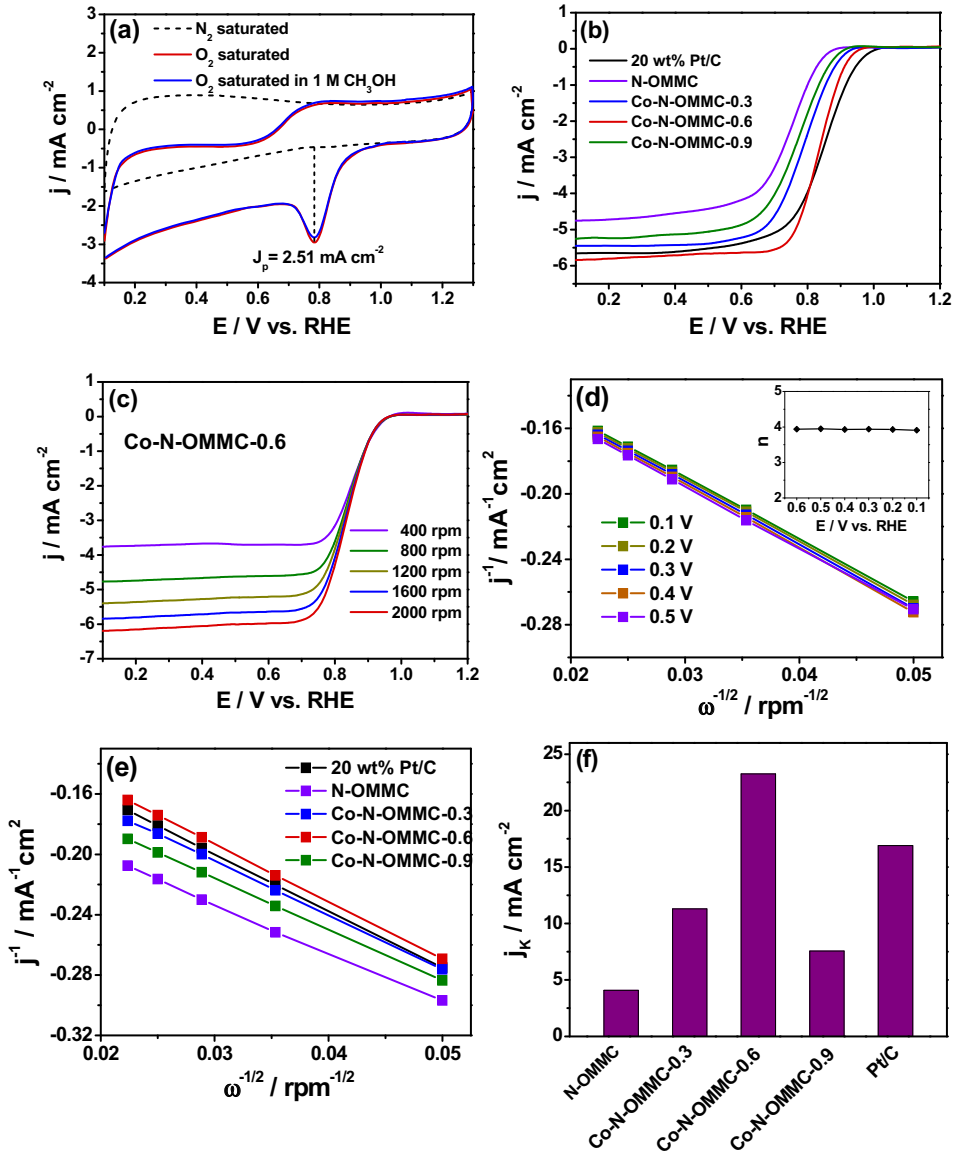

Fig. 5. (a) CVs of Co-N-OMMC-0.6 in O_2-or N_2-saturated 0.1 M KOH solutions as well as O_2-saturated 0.1 M KOH solution with 1 M CH_3OH. (b) LSVs of all studied samples at 1600 rpm and 5 mV s^{-1}. (c) Polarization curves of Co-N-OMMC-0.6 at different rotating speeds. (d) Koutecky–Levich plots of Co-N-OMMC-0.6 at different electrode potentials obtained from (c). The inset shows the dependence of electron transfer numbers (n) on the potential. (e) K–L plots of the ORR at 0.5 V vs. RHE from all studied catalysts. (f) Electrochemical activity given as the kinetic current density (j_k) at 0.75 V vs. RHE for all the studied samples.

0.6 manifests the best ORR activity among all the Co-N-OMMC catalysts and even a higher diffusion-limited current density than Pt/C, indicating a large quantity of exposed active sites on the Co-N-OMMC-0.6 catalyst. Additionally, Co-N-OMMC-0.6 provides a highly positive ORR half-wave potential of ~0.83 V vs. RHE, which is only ~0.01 V deviation from the Pt/C catalyst (~0.84 V vs. RHE). This half-wave potential (~0.83 V vs. RHE) of Co-N-OMMC-0.6 is also more positive than or comparable to that of the other reported non-precious metal ORR catalysts (Table S1), demonstrating an excellent ORR electrocatalytic activity of the Co-N-OMMC-0.6. The relatively worse ORR performance of Co-N-OMMC-0.9 compared with other Co-N-OMMC-x catalysts may be mainly related to the decreased surface area and the damage of the mesoporous structure (Fig. S1f) of the Co-N-OMMC-0.9 resulting from the excessive Co doping [15,53].

RDE tests were further performed from 400 to 2000 rpm to examine the reaction kinetics of all studied catalysts (Fig. 5c, Fig. S3). The limiting current density increases with increasing rotation speed, indicates a reduced diffusion distance at higher speeds [35]. The corresponding Koutecky–Levich (K–L) plots within the potential range from 0.1 to 0.5 V vs. RHE show good linearity with stable slopes, suggesting first order reaction kinetics towards ORR with respect to the concentration of dissolved oxygen (Fig. 5d, Fig. S4). The kinetic parameters for these samples including the electron-transfer numbers (n) and the kinetic currents (j_k) were calculated according to the Koutecky–Levich equation (see Section 2 for details). The K-L plots (Fig. 5e) give n = 3.9 at 0.5 V vs. RHE for Co-N-OMMC-0.6, revealing that the Co-N-OMMC-0.6 favors a 4e oxygen reduction process and O_2 is reduced to OH^-, which is same with Pt/C. In contrast, the electron transfer numbers of Co-N-OMMC-0.3, Co-N-OMMC-0.9, and N-OMMC at 0.5 V vs. RHE are 3.6, 3.4, and 3.1, respectively. As shown in Fig. 5f, the j_k value at 0.75 V vs. RHE for Co-N-OMMC-0.6 is determined to be 23.2 mA cm^{-2}, which is much higher than that of other studied catalysts. The outstanding ORR activity for the Co-N-OMMC-0.6 could be attributed to the homogeneously distributed, numerous Co-N_x active sites, large

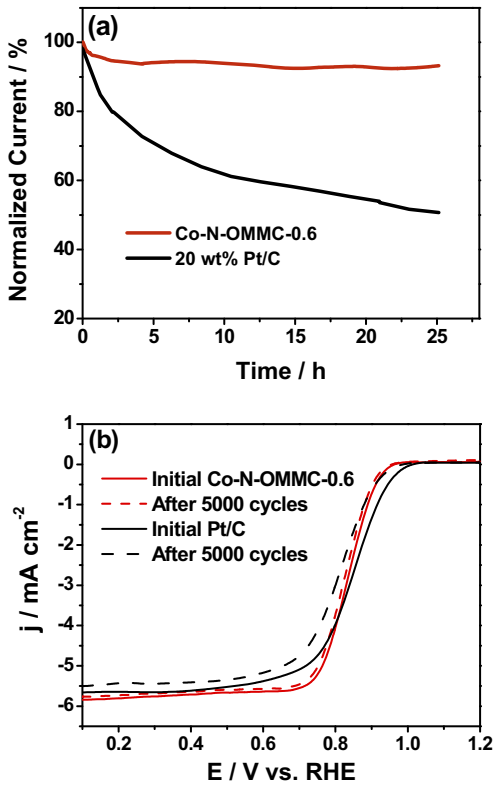

Fig. 6. (a) Retention percentage of the catalytic current of Co-N-OMMC-0.6 and Pt/C in O_2-saturated 0.1 M KOH solution. (b) LSVs of Co-N-OMMC-0.6 and Pt/C initially and after 5000 CV sweeps between 0.10 and 1.20 V vs. RHE.

number of exposed active sites from the high surface area mesopores, as well as facilitated mass transport of molecules and ions from the 3D ordered interconnected macro/mesoporous structure for increasing the accessibility to the active sites [51,54–57].

Durability is also of great significance for the practical utilization of an electrocatalyst. As seen in Fig. 6a, the chronoamperomogram of the Co-N-OMMC-0.6 shows negligible performance attenuation after 25 h of continuous operation at 0.5 V vs. RHE, in contrast to a sharp activity loss of commercial Pt/C, demonstrating the high stability of Co-N-OMMC-0.6 for ORR. The stability was also evaluated by cycling the electrode potential between 0.2 and 1.0 V vs. RHE at a scan rate of 100 mV s^{-1} in O_2 saturated 0.1 M KOH solution (Fig. 6b). After 5000 continuous cycles, the half-wave potential of the Co-N-OMMC-0.6 shifted negatively by only 3 mV, much less than that of the Pt/C catalyst (24 mV), indicating the outstanding catalytic durability of the Co-N-OMMC-0.6. Such a super electrochemical stability of the prepared Co-N-OMMC-0.6 catalyst might arise from the homogeneous incorporation of the active sites into the carbon matrix. Even though degradation occurs on the surface of the catalyst, the new active sites are exposed and thereby the activity of the catalyst remains high [51,58]. In addition, the Co-N-OMMC-0.6 catalyst shows perfect ORR selectivity in methanol-containing electrolyte, whereas a significantly high methanol oxidation current is observed for the Pt/C catalyst under the same conditions (Fig. 5a, Fig. S5).

4. Conclusion

In summary, cobalt-nitrogen-doped 3D ordered macro-/mesoporous carbons (Co-N-OMMCs) have been successfully synthesized by a facile dual-templating approach using silica opal as a macroporous template and triblock copolymer Pluronic F127 as a mesopore-structure-directing agent. The optimal Co-N-OMMC-0.6 catalyst exhibits a well-defined mesoporous structure on the ordered macroporous walls and has a high BET surface area of 635 m^2 g^{-1}. Attributing to the merit of highly active Co-N_x species and the structural advantages of the 3D ordered interconnected macropores and mesopores, such as enlarged exposure of catalytically active sites, improved mass/charge transport, and high structural stability, the Co-N-OMMC-0.6 displays high ORR activity through a four-electron reduction process with a half-wave potential of 0.83 V vs. RHE. Furthermore, the Co-N-OMMC-0.6 catalyst shows greatly enhanced ORR catalytic durability and methanol tolerance compared to the commercial Pt/C catalyst. The superior electrocatalytic performance indicates that the Co-N-OMMC-0.6 is a promising candidate for cathode catalysts in fuel cells. In addition, the present method could potentially be used for fabricating other transition-metal-nitrogen doped carbon materials with similar 3D ordered macro-/mesoporous structure.

Acknowledgements

The authors gratefully acknowledge financial support from the National Natural Science Foundation of China (51172014), and Open Project of the State Key Laboratory of Organic–Inorganic Composites (oic-201601003).

Appendix A. Supplementary data

Supplementary data associated with this article can be found, in the online version, at http://dx.doi.org/10.1016/j.apcatb.2016.04.006.

References

[1] Q. Zhang, E. Uchaker, S.L. Candelaria, G. Cao, Chem. Soc. Rev. 42 (2013) 3127–3171.
[2] I. Katsounaros, S. Cherevko, A.R. Zeradjanin, K.J.J. Mayrhofer, Angew. Chem. Int. Ed. 53 (2014) 102–121.
[3] W. Ai, Z. Luo, J. Jiang, J. Zhu, Z. Du, Z. Fan, L. Xie, H. Zhang, W. Huang, T. Yu, Adv. Mater. 26 (2014) 6186–6192.
[4] Y. Liang, Y. Li, H. Wang, H. Dai, J. Am. Chem. Soc. 135 (2013) 2013–2036.
[5] J. Liu, L. Jiang, Q. Tang, E. Wang, L. Qi, S. Wang, G. Sun, Appl. Catal. B: Environ. 148–149 (2014) 212–220.
[6] H. Tang, H. Yin, J. Wang, N. Yang, D. Wang, Z. Tang, Angew. Chem. Int. Ed. 52 (2013) 5585–5589.
[7] K. Asazawa, H. Kishi, H. Tanaka, D. Matsumura, K. Tamura, Y. Nishihata, A.G. Saputro, H. Nakanishi, H. Kasai, K. Artyushkova, P. Atanassov, J. Phys. Chem. C 118 (2014) 25480–25486.
[8] T.S. Olson, S. Pylypenko, P. Atanassov, K. Asazawa, K. Yamada, H. Tanaka, J. Phys. Chem. C 114 (2010) 5049–5059.
[9] H.-H. Li, S.-Y. Ma, Q.-Q. Fu, X.-J. Liu, L. Wu, S.-H. Yu, J. Am. Chem. Soc. 137 (2015) 7862–7868.
[10] H.-W. Liang, X. Cao, F. Zhou, C.-H. Cui, W.-J. Zhang, S.-H. Yu, Adv. Mater. 23 (2011) 1467–1471.
[11] M. Nesselberger, M. Roefzaad, R. Fayçal Hamou, P. Ulrich Biedermann, F.F. Schweinberger, S. Kunz, K. Schloegl, G.K.H. Wiberg, S. Ashton, U. Heiz, K.J.J. Mayrhofer, M. Arenz, Nat. Mater. 12 (2013) 919–924.
[12] Y. Nie, L. Li, Z. Wei, Chem. Soc. Rev. 44 (2015) 2168–2201.
[13] Y. Tan, C. Xu, G. Chen, X. Fang, N. Zheng, Q. Xie, Adv. Funct. Mater. 22 (2012) 4584–4591.
[14] P. Ganesan, M. Prabu, J. Sanetuntikul, S. Shanmugam, ACS Catal. 5 (2015) 3625–3637.
[15] D.-S. Yang, D. Bhattacharjya, S. Inamdar, J. Park, J.-S. Yu, J. Am. Chem. Soc. 134 (2012) 16127–16130.
[16] J. Liang, Y. Zheng, J. Chen, J. Liu, D. Hulicova-Jurcakova, M. Jaroniec, S.Z. Qiao, Angew. Chem. Int. Ed. 51 (2012) 3892–3896.
[17] D. Liu, X. Zhang, Z. Sun, T. You, Nanoscale 5 (2013) 9528–9531.
[18] Q. Tang, L. Jiang, J. Liu, S. Wang, G. Sun, ACS Catal. 4 (2014) 457–463.
[19] W. Xia, R. Zou, L. An, D. Xia, S. Guo, Energy Environ. Sci. 8 (2015) 568–576.
[20] Z.-S. Wu, L. Chen, J. Liu, K. Parvez, H. Liang, J. Shu, H. Sachdev, R. Graf, X. Feng, K. Müllen, Adv. Mater. 26 (2014) 1450–1455.
[21] L. Dai, Y. Xue, L. Qu, H.-J. Choi, J.-B. Baek, Chem. Rev. 115 (2015) 4823–4892.
[22] A. Zahoor, M. Christy, Y.J. Hwang, Y.R. Lim, P. Kim, K.S. Nahm, Appl. Catal. B: Environ. 147 (2014) 633–641.
[23] L.-F. Chen, X.-D. Zhang, H.-W. Liang, M. Kong, Q.-F. Guan, P. Chen, Z.-Y. Wu, S.-H. Yu, ACS Nano 6 (2012) 7092–7102.
[24] H.T. Chung, J.H. Won, P. Zelenay, Nat. Commun. 4 (2013) 1922.

[25] J. Xiao, X. Bian, L. Liao, S. Zhang, C. Ji, B. Liu, ACS Appl. Mater. Interfaces 6 (2014) 17654–17660.
[26] K. Wan, G.-F. Long, M.-Y. Liu, L. Du, Z.-X. Liang, P. Tsiakaras, Appl. Catal. B: Environ. 165 (2015) 566–571.
[27] X. Sheng, N. Daems, B. Geboes, M. Kurttepeli, S. Bals, T. Breugelmans, A. Hubin, I.F.J. Vankelecom, P.P. Pescarmona, Appl. Catal. B: Environ. 176–177 (2015) 212–224.
[28] Y.-L. Liu, C.-X. Shi, X.-Y. Xu, P.-C. Sun, T.-H. Chen, J. Power Sources 283 (2015) 389–396.
[29] H. Zhong, C. Deng, Y. Qiu, L. Yao, H. Zhang, J. Mater. Chem. A 2 (2014) 17047–17057.
[30] Y. Chen, R. Ma, Z. Zhou, G. Liu, Y. Zhou, Q. Liu, S. Kaskel, J. Wang, Adv. Mater. Interfaces 2 (2015) 1500199.
[31] J. Liang, X. Du, C. Gibson, X.W. Du, S.Z. Qiao, Adv. Mater. 25 (2013) 6226–6231.
[32] G. Tao, L. Zhang, L. Chen, X. Cui, Z. Hua, M. Wang, J. Wang, Y. Chen, J. Shi, Carbon 86 (2015) 108–117.
[33] J. Han, Y.J. Sa, Y. Shim, M. Choi, N. Park, S.H. Joo, S. Park, Angew. Chem. Int. Ed. 54 (2015) 12622–12626.
[34] C.W.B. Bezerra, L. Zhang, K. Lee, H. Liu, A.L.B. Marques, E.P. Marques, H. Wang, J. Zhang, Electrochim. Acta 53 (2008) 4937–4951.
[35] H. Jiang, Y. Su, Y. Zhu, J. Shen, X. Yang, Q. Feng, C. Li, J. Mater. Chem. A 1 (2013) 12074–12081.
[36] S. Chao, Q. Cui, K. Wang, Z. Bai, L. Yang, J. Qiao, J. Power Sources 288 (2015) 128–135.
[37] C.M.A. Parlett, K. Wilson, A.F. Lee, Chem. Soc. Rev. 42 (2013) 3876–3893.
[38] C. Zhang, L. Xu, N. Shan, T. Sun, J. Chen, Y. Yan, ACS Catal. 4 (2014) 1926–1930.
[39] A.A. Zakhidov, R.H. Baughman, Z. Iqbal, C.X. Cui, I. Khayrullin, S.O. Dantas, J. Marti, V.G. Ralchenko, Science 282 (1998) 897.
[40] Y. Meng, D. Gu, F. Zhang, Y. Shi, H. Yang, Z. Li, C. Yu, B. Tu, D. Zhao, Angew. Chem. Int. Ed. 44 (2005) 7053–7059.
[41] Y. Jiang, Y. Lu, X. Wang, Y. Bao, W. Chen, L. Niu, Nanoscale 6 (2014) 15066–15072.
[42] H.-J. Liu, W.-J. Cui, L.-H. Jin, C.-X. Wang, Y.-Y. Xia, J. Mater. Chem. 19 (2009) 3661–3667.
[43] K.S.W. Sing, D.H. Everett, R.A.W. Haul, L. Moscou, R.A. Pierotti, J. Rouquerol, T. Siemieniewska, Pure Appl. Chem. 57 (1985) 603–619.
[44] S.R. Kelemen, M. Afeworki, M.L. Gorbaty, P.J. Kwiatek, J. Energy Fuels 16 (2002) 1507–1515.
[45] Y. Nabae, S. Moriya, K. Matsubayashi, S.M. Lyth, M. Malon, L. Wu, N.M. Islam, Y. Koshigoe, S. Kuroki, M.-a. Kakimoto, S. Miyata, J.-i. Ozaki, Carbon 48 (2010) 2613–2624.
[46] G. Wu, C.M. Johnston, N.H. Mack, K. Artyushkova, M. Ferrandon, M. Nelson, J.S. Lezama-Pacheco, S.D. Conradson, K.L. More, D.J. Myers, P. Zelenay, J. Mater. Chem. 21 (2011) 11392–11405.
[47] Y. Zhu, B. Zhang, X. Liu, D.-W. Wang, D.S. Su, Angew. Chem. Int. Ed. 53 (2014) 10673–10677.
[48] Y. Su, H. Jiang, Y. Zhu, X. Yang, J. Shen, W. Zou, J. Chen, C. Li, J. Mater. Chem. A 2 (2014) 7281–7287.
[49] Y. Zhao, K. Watanabe, K. Hashimoto, J. Am. Chem. Soc. 134 (2012) 19528–19531.
[50] H. Huang, Q. Wang, Q. Wei, Y. Huang, Int. J. Hydrogen Energy 40 (2015) 6072–6084.
[51] H.-W. Liang, W. Wei, Z.-S. Wu, X. Feng, K. Müllen, J. Am. Chem. Soc. 135 (2013) 16002–16005.
[52] Z. Li, G. Li, L. Jiang, J. Li, G. Sun, C. Xia, F. Li, Angew. Chem. Int. Ed. 54 (2015) 1494–1498.
[53] M. Li, X. Bo, Y. Zhang, C. Han, A. Nsabimana, L. Guo, J. Mater. Chem. A 2 (2014) 11672–11682.
[54] T. Sun, C. Zhang, J. Chen, Y. Yan, A.A. Zakhidov, R.H. Baughman, L. Xu, J. Mater. Chem. A 3 (2015) 11367–11375.
[55] O.-H. Kim, Y.-H. Cho, S.H. Kang, H.-Y. Park, M. Kim, J.W. Lim, D.Y. Chung, M.J. Lee, H. Choe, Y.-E. Sung, Nat. Commun. 4 (2013) 2473.
[56] J.Y. Cheon, T. Kim, Y.M. Choi, H.Y. Jeong, M.G. Kim, Y.J. Sa, J. Kim, Z. Lee, T.-H. Yang, K. Kwon, O. Terasaki, G.-G. Park, R.R. Adzic, S.H. Joo, Sci. Rep. 3 (2013) 2715.
[57] A. Kong, X. Zhu, Z. Han, Y. Yu, Y. Zhang, B. Dong, Y. Shan, ACS Catal. 4 (2014) 1793–1800.
[58] A. Sarapuu, L. Samolberg, K. Kreek, M. Koel, L. Matisen, K. Tammeveski, J. Electroanal. Chem. 746 (2015) 9–17.